



1 Scenario-driven ozone projections and associated impact
2 on mortality over Africa with an integrated machine
3 learning framework

4
5
6 Huimin Li¹, Yang Yang^{2, 3*}, Hailong Wang⁴

7
8 ¹School of Environment and Ecology, Jiangsu Open University, Nanjing,
9 Jiangsu, China

10 ²State Key Laboratory of Climate System Prediction and Risk
11 Management/Jiangsu Key Laboratory of Atmospheric Environment Monitoring
12 and Pollution Control/Jiangsu Collaborative Innovation Center of Atmospheric
13 Environment and Equipment Technology/Joint International Research
14 Laboratory of Climate and Environment Change, Nanjing University of
15 Information Science and Technology, Nanjing, Jiangsu, China

16 ³School of Environmental Science and Engineering, Nanjing University of
17 Information Science and Technology, Nanjing, Jiangsu, China

18 ⁴Atmospheric, Climate, and Earth Sciences Division, Pacific Northwest
19 National Laboratory, Richland, Washington, USA

20

21

22 *Correspondence to yang.yang@nuist.edu.cn

23



24 **Abstract**

25 Ozone (O₃), a major tropospheric air pollutant, poses significant threats to
26 public health and ecosystems, especially across Africa, where O₃
27 concentrations have experienced pronounced increases in recent decades.
28 This study employs an interpretable machine learning (ML) model integrated
29 with multi-source data to predict near-surface O₃ levels over Africa from 2020
30 to 2050 driven by climate change under four Shared Socioeconomic Pathways
31 (SSPs). We quantitatively investigate the respective roles of climate-driven
32 changes in meteorological conditions and biogenic isoprene emissions in
33 affecting future O₃ variations. Results reveal that as a NO_x-limited region,
34 increased biogenic isoprene emissions contribute to a slight reduction in O₃
35 levels (< 0.5 ppb). Conversely, favorable meteorological conditions elevate O₃
36 levels over Africa, with a maximum projected increase of 2.0 ppb in 2050
37 relative to 2020, dominating the O₃ variations driven by climate change. The
38 low-emission SSP scenarios are projected to prompt less increases in O₃ levels
39 than the high-emission SSPs. Moreover, elevated air temperatures associated
40 with global warming magnify the health burden across Africa, as O₃ pollution
41 acts as an additional stressor in a warming climate. This highlights the urgency
42 for robust air pollution control and climate mitigation strategies to alleviate future
43 health impacts in Africa.



44 **1. Introduction**

45 Ozone (O_3) near the surface is a secondary air pollutant, primarily
46 generated via the complex photochemical reactions involving precursors such
47 as nitrogen oxides ($NO_x = NO + NO_2$) and volatile organic compounds (VOCs)
48 under solar radiation. Since O_3 absorbs longwave radiation, it also acts as an
49 important greenhouse gas that contributes to climate forcing (Myhre et al.,
50 2017). Chronic exposure to elevated O_3 levels poses substantial threats to
51 human health (Anenberg et al., 2010; Lelieveld et al., 2015), ecosystems (Yue
52 et al., 2017; Mills et al., 2018), and climate change (Gaudel et al., 2018; Gao et
53 al., 2022; Wang et al., 2023). Africa suffers a high burden of O_3 pollution in
54 densely populated regions, where exhibit a rapid increase in daily maximum 8
55 h mean (MDA8) O_3 with an annual growth rate exceeding 3% (Sicard et al.,
56 2023). Approximately more than 0.3 million premature deaths are attributed to
57 O_3 pollution in 2019, which has become the second largest cause of death in
58 Africa (Fisher et al., 2021; Lyu et al., 2023). Therefore, it is urgent to
59 characterize the long-term variations of O_3 over Africa and identify their
60 underlying driving factors.

61 Two thirds of countries in Africa lack ground-based observational data with
62 sufficient temporal and geographic coverage, making it difficult to evaluate the
63 air quality across the entire continent (Fajersztajn et al., 2014). Satellite O_3
64 products from the Total Ozone Mapping Spectrometer can provide long-time
65 series of data. Combined these satellite measurements with the Global



66 Modeling Initiative model, Ziemke et al. (2019) found a 4–5 DU (Dobson unit)
67 increase in tropospheric column O_3 over Central Africa during the past four
68 decades. Nevertheless, these satellite retrievals still face spatial gaps and
69 accuracy challenges, and cannot be directly used to estimate chemical and
70 physical processes involved in O_3 production and loss (Colombi et al., 2021;
71 Miyazaki et al., 2025). To complement the limitations of near-surface O_3
72 measurements, chemical transport models (CTMs) have been applied to
73 simulate O_3 concentrations. Zunckel et al. (2006) found that the modelled near-
74 surface O_3 mixing ratio over Southern Africa frequently exceeded 40 ppb, which
75 may damage the local crops. Currently, artificial intelligence algorithms such as
76 machine learning (ML) methods are widely applied in O_3 research due to their
77 high computational efficiency and strong predictive performance, which can
78 contribute to reducing the simulation biases inherent in traditional CTMs
79 (Requia et al., 2020; Z. Liu et al., 2022; Wei et al., 2022; Li et al., 2023, 2024;
80 Ni et al., 2024). For example, X. Liu et al. (2022) developed a 0.5° global
81 monthly near-surface O_3 dataset for the period of 2003–2019 based on a
82 cluster-enhanced ensemble ML method, and demonstrated that the average
83 population-weighted MDA8 O_3 concentration in Northern Africa reached 53 ppb
84 during the peak season, exceeding the global average of 47 ppb. Due to the
85 severe O_3 pollution in Africa, the prediction of future O_3 concentrations is
86 essential to providing scientific guidance for effective mitigation strategies.

87 The variation of O_3 largely depends on meteorological factors and synoptic



88 conditions (Jacob and Winner, 2009; Doherty et al., 2013; Kavassalis and
89 Murphy, 2017; Fu and Tian, 2019; Gong and Liao, 2019; Lu et al., 2019; Yang
90 et al., 2022; Li et al., 2023, 2024). As documented in the Sixth Assessment
91 Report of the Intergovernmental Panel on Climate Change (IPCC AR6), all
92 global regions would experience intensified climate change, with the frequency,
93 intensity, and duration of heatwaves are projected to increase by 2100 (IPCC,
94 2021). The frequency of high-temperature days in Africa is projected to increase
95 substantially by the mid-21st century under the Shared Socioeconomic
96 Pathway (SSP) 2-4.5 (26–59%) and SSP5-8.5 (30–69%) relative to the recent
97 climatology of 1991–2010 (Iyakaremye et al., 2021). Such future climate
98 changes under the various scenarios will further influence near-surface O₃
99 through altering meteorological factors (Colette et al., 2015; Wang et al., 2022).
100 Turnock et al. (2022) applied the United Kingdom Earth System Model
101 (UKESM1) to assess the impacts of future climate change on near-surface O₃,
102 and found a modest reduction in annual mean O₃ levels by 2050 across
103 Northern Africa (4%) and Southern Africa (2%) under the SSP3-7.0 scenario.
104 Compound events involving extremely high temperatures and O₃
105 concentrations are projected to occur more frequently, with Africa experiencing
106 the largest increase of compound-event days by more than 150 days in 2080s
107 under the SSP5-8.5 scenario compared to the baseline of 1995–2014 (Ban et
108 al., 2022). Utilizing three state-of-the-art earth system models, Brown et al.
109 (2022) showed a multi-model average increase of O₃ by up to 4 ppb over urban



110 areas of Africa during 2090–2100 under the SSP3-7.0 scenario.

111 Variations in meteorological parameters under the SSP scenarios can also

112 influencing O₃ levels through perturbing natural emissions of precursors, such

113 as those from vegetation, soil and lightning. As a dominant O₃ precursor, VOCs

114 are largely emitted from terrestrial ecosystems (Kesselmeier and Staudt, 1999),

115 with approximately 90% originating from biogenic sources (Guenther et al.,

116 1995). Wang, Li et al. (2025) evaluated annual O₃ precursor emissions in 2019

117 over Southern Africa from different emission inventories, and demonstrated that

118 biogenic VOCs (BVOCs) emissions exceeded those from other sources by a

119 factor of 9 to 147. Among BVOCs, isoprene contributes the largest proportion

120 of total emissions (Guenther et al., 2012). Notably, the African continent

121 accounts for 20% of global isoprene emissions, with the evergreen tropical

122 forests of Western and Equatorial Africa serving as a major source (Marais et

123 al., 2012; Jaars et al., 2016; Sindelarova et al., 2022). Evidences indicate that

124 BVOCs emissions are strongly modulated by meteorological conditions, such

125 as air temperature, solar radiation, relative humidity, and precipitation (Zhang

126 et al., 2008; Debevec et al., 2018; Yáñez-Serrano et al., 2020; Liu et al., 2021).

127 Given the potentially increasing variability in future climate, isoprene emissions

128 are becoming more uncertain in O₃ prediction, as it plays a crucial role in

129 tropospheric chemistry, particularly in the formation of tropospheric O₃

130 (Fehsenfeld et al., 1992; Williams et al., 2009). Consequently, future changes

131 in isoprene emissions in a warming climate are expected to further impact O₃



132 concentrations across Africa.

133 Many previous studies predicted future O₃ under single scenario based on
134 limited climate model simulations, without considering the impacts of climate
135 change on O₃ variations, as well as the underlying changing meteorological
136 conditions and natural precursor emissions. Also, the uncertainties in future
137 meteorological parameters projected by a small number of climate models can
138 also suffer specific model biases in O₃ predictions. In this study, we aim to
139 quantify the impacts of future climate change on near-surface O₃ concentrations
140 over Africa in the mid-21st century (average of 2045–2054) by employing a ML
141 approach integrated with GEOS-Chem model simulations and multi-model
142 simulations under four SSPs scenarios (SSP1-2.6, SSP2-4.5, SSP3-7.0, and
143 SSP5-8.5) from the Coupled Model Intercomparison Project Phase 6 (CMIP6).
144 Individual contributions of changing meteorological conditions and changing
145 natural emissions (isoprene) under climate change are separately evaluated.
146 The corresponding future health risk in Africa is also assessed. Details of the
147 data, model description and methodology are elaborated in Sect. 2. Section 3
148 presents future projections of near-surface O₃ concentrations over Africa,
149 relative contributions of driving factors, and assessment of the health risks. Key
150 conclusions and potential uncertainties of this study are summarized in Sect. 4.

151 **2. Materials and methods**

152 **2.1 GEOS-Chem model simulations**

153 The historical near-surface O₃ concentrations over Africa (36°S–30°N,



154 17.5°W–50°E) for the period 2000–2019 are simulated in the GEOS-Chem
155 model version 13.4.1, which is driven by meteorological fields from the Modern-
156 Era Retrospective analysis for Research and Applications version 2 (MERRA-
157 2; Gelaro et al., 2017). The model simulation has a horizontal resolution of 2°
158 latitude × 2.5° longitude, and includes 47 vertical layers from the surface up to
159 0.01 hPa. It incorporates fully coupled O₃-NO_x-hydrocarbon-aerosol chemical
160 mechanisms (Park et al., 2004; Pye et al., 2009; Mao et al., 2013), with about
161 300 species participating in over 400 kinetic and photochemical reactions (Bey
162 et al., 2001). Vertical mixing process within the planetary boundary layer is
163 characterized using a non-local scheme (Lin and McElroy, 2010), and
164 stratospheric O₃ chemistry utilizes the linearized O₃ parameterization scheme
165 (LINOZ; McLinden et al., 2000).

166 Anthropogenic emissions of O₃ precursors, including non-methane VOCs
167 (NMVOCs), NO_x and CO from 2000 to 2019 are derived from the Community
168 Emissions Data System (CEDS) version 2021_04_21 (O'Rourke et al., 2021).
169 Biogenic emissions are calculated online based on the Model of Emissions of
170 Gases and Aerosols from Nature (MEGAN) version 2.1 (Guenther et al. 2012).
171 Biomass burning emissions are obtained from the Global Fire Emissions
172 Database (GFED) version 4 (van der Werf et al., 2017). NO_x emissions from
173 soil sources are estimated online according to an updated version of the
174 Berkeley–Dalhousie Soil NO_x Parameterization scheme proposed by Hudman
175 et al. (2012). Lightning-induced NO_x emissions are calculated online following



176 the algorithm developed by Ott et al. (2010) and Murray et al. (2012). Methane
177 (CH₄) concentrations are prescribed using spatially interpolated monthly
178 average observations from the National Oceanic and Atmospheric
179 Administration (NOAA) Global Monitoring Division (GMD; Murray, 2016).
180 Previous studies have shown that GEOS-Chem model well reproduces the
181 magnitude and spatial distributions of observed O₃ concentrations across Africa
182 (Han et al., 2018; Yan et al., 2019; Wang, Li et al., 2025).

183 **2.2 CMIP6 multi-model outputs**

184 The CMIP6 repository contains multi-model climate projections for various
185 SSPs based on alternative scenarios of future emissions and land use changes
186 (O'Neill et al., 2016). In this study, we collect meteorological variables from
187 CMIP6 models under four different scenarios. SSP1-2.6 represents a low-
188 forcing scenario that considers comprehensive climate mitigation strategies to
189 effectively reduce greenhouse gas emissions and progress toward sustainable
190 development goals. SSP2-4.5 is an intermediate-forcing scenario that follows
191 the business-as-usual pathway. SSP3-7.0 corresponds to a medium-to-high
192 forcing scenario. SSP5-8.5 denotes a high-forcing scenario aiming to achieve
193 climate adaptation alongside rapid development through intensive utilization of
194 fossil-fueled resources.

195 To perform a robust prediction of future near-surface O₃ concentrations in
196 Africa, climate projections from 18 global climate models participating in CMIP6
197 are applied, including ACCESS_CM2, ACCESS-ESM1-5, CanESM5, CESM2-



198 WACCM, CMCC-CM2-SR5, EC-Earth3, EC-Earth3-Veg, FGOALS-f3-L,
199 FGOALS-g3, GFDL-ESM4, INM-CM5-0, IPSL-CM6A-LR, MIROC6, MPI-
200 ESM1-2-HR, MPI-ESM1-2-LR, MRI-ESM2-0, NorESM2-LM, and NorESM2-
201 MM. These models provide the major meteorological variables essential for
202 predicting near-surface O₃, such as air temperatures (at 2m, 850 hPa, and 500
203 hPa), wind fields (at 850 hPa and 500 hPa), incoming shortwave radiation at
204 the surface, near-surface relative humidity, precipitation rate, total cloud cover,
205 and sea level pressure under the four different scenarios. In order to minimize
206 the inconsistencies of initial conditions between CMIP6 models and MERRA-2
207 reanalysis data, the future meteorological fields under different scenarios from
208 CMIP6 models are adjusted based on the differences between CMIP6 historical
209 meteorological variables and MERRA-2 reanalysis data during 2000–2019
210 following H. Li et al. (2022, 2023, 2024). Additionally, to discuss the role of
211 climate change in the projected variation of O₃ concentrations driven mainly by
212 anthropogenic emissions, the monthly O₃ simulation outputs under four SSPs
213 scenarios from 8 CMIP6 models are adopted, including BCC-CSM2-MR,
214 FGOALS-g3, IPSL-CM6A-LR, MPI-ESM1-2-HR, MPI-ESM1-2-LR, MRI-ESM2-
215 0, NorESM2-LM, and NorESM2-MM.

216 **2.3 Machine learning model construction**

217 As one of the traditional ML algorithms, Random Forest (RF) model can
218 process high-dimensional data with lower computational costs compared to the
219 CTMs (Breiman et al., 2001). This ensemble approach excels at dealing with



220 nonlinear and complex relationships between input and target variables, and it
221 provides stable and reliable predictions of O_3 in many previous studies (Wei et
222 al., 2022; Xu et al., 2023). In this study, to predict future near-surface O_3 over
223 Africa, we integrate a set of relevant features as predictors, including O_3
224 concentrations from GEOS-Chem model simulations, O_3 precursor emissions,
225 meteorological variables, topography (TOPO), land cover (LC), normalized
226 difference vegetation index (NDVI), and population density (POP). Considering
227 the autocorrelation between O_3 and its covariates varies across space and time,
228 the RF model also incorporates spatiotemporal information, including month of
229 the year (MOY), longitude (LON) and latitude (LAT) across the Africa domain.
230 The details of input data applied in this study are summarized in Table 1.

231 Here we firstly predict future biogenic isoprene emissions based on RF
232 model, which are then used for predicting future near-surface O_3 concentrations
233 across Africa. The RF model for isoprene is trained by the emission output from
234 MEGAN2.1 in GEOS-Chem model, MERRA-2 meteorological variables, TOPO,
235 LC, NDVI, POP, MOY, LAT, and LON over 2000–2009 and 2011–2019. The
236 2010 records are used to validate the performance of RF model, as that land
237 surface air temperature over Africa reached its peak during 2000–2019, which
238 facilitates future projections in a warming climate. This data splitting strategy
239 ensures the critical information related to rising temperature trends is captured
240 in both RF model training and testing phases. Based on trained RF model, the
241 future monthly isoprene emissions from 2020 to 2054 under different climate



242 scenarios (SSP1-2.6, SSP2-4.5, SSP3-7.0, and SSP5-8.5) in Africa are then
243 predicted using future meteorological fields from CMIP6.

244 Secondly, to train the RF model for predicting future monthly near-surface
245 O₃ concentrations in Africa, we composite O₃ simulations from GEOS-Chem
246 model, emissions and concentrations of O₃ precursors, the ratio of VOCs
247 emission to NO_x emission, MERRA-2 meteorological variables, and auxiliary
248 data. The ratio of VOCs emission to NO_x emission is used to roughly determine
249 the ozone formation regime. The samples over 2000–2009 and 2011–2019 are
250 selected as training dataset and the remaining data over 2010 as testing data.
251 We conduct two experiments to quantitatively estimate the direct (via altering
252 meteorological conditions) and indirect (via altering biogenic isoprene
253 emissions) effects of climate change on future O₃ in Africa. By feeding the
254 varying meteorological parameters into the trained model while fixing isoprene
255 emissions in 2020, the climate-driven O₃ variations through changing
256 meteorological conditions are explored (O₃_MET). Both the isoprene
257 projections and CMIP6 multi-model projections from 2020 to 2054 under four
258 scenarios are fed to the trained RF model to predict O₃ (O₃_ALL), and the
259 difference of O₃_ALL – O₃_MET represents the impacts of changing isoprene
260 emissions under climate change (O₃_NAT).

261 The RF model's predictive performance was optimized through
262 hyperparameter tuning. The best hyperparameters (n_estimators = 600,
263 min_samples_split = 2, max_features = "sqrt", bootstrap = "True") of RF model



for predicting isoprene emissions and O₃ concentrations are tuned separately by 10-fold cross-validation (Rodriguez et al., 2010). To assess the accuracy of RF model, statistical metrics such as coefficient of determination (R²), mean absolute error (MAE), root mean square error (RMSE), and mean relative error (MRE) are calculated by comparing the outputs of RF model and GEOS-Chem model. Moreover, we employ the Shapley Additive explanation (SHAP) approach (Lundberg and Lee, 2017) to quantify the importance of individual factors determining the RF model's predictions. The SHAP provides a value that reflects the contribution of each input variable to specific predictions, and has been widely adopted in atmospheric environmental studies to enhance the interpretability of the ML model (Hou et al., 2022; Stinberg et al., 2021).

2.4 Mortality burden assessment

Exposure to elevated temperatures and O₃ pollution, exacerbated by global warming, significantly increases human health risks. We assess the future mortality ratio (MR) attributable to ambient O₃ and temperature changes, respectively, under different scenarios in Africa from 2020 to 2054, using the following equations:

$$MR_{ozone} = \frac{\frac{\sum_i RR_{ozone,i}}{m}}{\frac{\sum_j RR_{ozone,j}}{n}} \quad (1)$$

$$MR_{temperature} = \frac{\frac{\sum_i RR_{temperature,i}}{m}}{\frac{\sum_j RR_{temperature,j}}{n}} \quad (2)$$

$$RR_{ozone} = \exp(\beta_1(C - C_0)) \quad (3)$$



$$RR_{temperature} = \exp(\beta_2(T-T_0)) \quad (4)$$

where MR_{ozone} ($MR_{temperature}$) stands for the MR due to O_3 pollution (temperature) changes. $RR_{ozone,i}$ and $RR_{temperature,i}$ represent relative risks caused by O_3 and temperature exceedance in a future (2050–2054) month i , respectively. $RR_{ozone,j}$ and $RR_{temperature,j}$ denote relative risk caused by O_3 and temperature exceedance on a baseline (2020–2024) month j , respectively. m is the total number of months during future period, and n is the total number of months of baseline period. β_1 indicates the O_3 concentration response factor, with a value of 1.39×10^{-3} (95% confidence interval: 8.9597×10^{-4} , 1.8822×10^{-3}) per ppb (Wang, Yang et al., 2025). C_0 is the theoretical minimum risk exposure level (TMREL) for O_3 exposure, which ranges from 29.1 to 35.7 ppb as adopted in Global Burden of Disease (GBD) 2019 study (2020). Following Malashock et al. (2022), we use the medium value of 32.4 ppb in this study. C reflects the O_3 concentrations predicted by the RF model. β_2 signifies the temperature response factor, and each 1°C increase in temperature over Africa is associated with a 1.3×10^{-2} (95% confidence interval: 0.4×10^{-2} , 2.2×10^{-2}) rise in mortality risk (Cromar et al., 2022). T_0 is the threshold value indicating minimum mortality temperature (MMT), an important indicator for characterizing the health impacts of global heating. The 50th percentile of temperature distribution corresponding to the MMT over Southern Africa was calculated to be 25°C , which is used as the reference value for this study (Tobías et al., 2021). T reflects air temperature from the CMIP6 dataset. Similar calculation



methodology has been applied in previous studies (Lee and Kim, 2016; Wang et al., 2022).

3. Results

3.1 Evaluation of machine learning model performance

We evaluate the ML model using a test dataset from year 2010. Figure 1(a) and (b) illustrates the consistency between RF model projections and GEOS-Chem model simulations for isoprene emissions and near-surface O₃ concentrations in Africa, respectively. The RF model exhibits a strong predictive capability in reproducing both isoprene emissions ($R^2 = 0.97$, MRE = 17%) and near-surface O₃ concentrations ($R^2 = 0.94$, MRE = 6%). These robust statistical metrics confirm the trained RF model's suitability for predicting future O₃ concentrations over Africa under a warmer climate.

The isoprene emissions simulated by GEOS-Chem model during 2000–2019 reveal apparent regional discrepancies across Africa (Figure 2a). The maximum isoprene emissions originate from evergreen broadleaf trees over Central Africa, which has the second largest tropical rainforest in the world. Southern Africa exhibits relatively lower isoprene emissions due to its sparse coverage of deciduous broadleaf trees. Northern Africa, dominated by deserts and semi-arid grasslands, contributes little to isoprene emissions. The isoprene projections estimated by the RF model perfectly capture the spatial distributions of isoprene emissions across Africa, with a correlation coefficient (R) between the RF projections and GEOS-Chem simulations of 0.99 and a normalized



mean bias (NMB) of -0.2%. In addition, the O₃ concentrations from 2000 to 2019 simulated by GEOS-Chem model indicate that O₃ pollution is predominantly concentrated in Southern Africa, as well as parts of Northern Africa and Central Africa, with concentrations over 40 ppb (Figure 2b). The RF model accurately reproduces this spatial characteristic, which aligns well with the O₃ simulation results ($R = 0.99$, $NMB = -0.02\%$).

To gain deeper insights into the driving factors behind RF model outputs, we utilize SHAP, an explainable artificial intelligence technique, to quantify the contribution of each feature to the projections of biogenic isoprene emissions (Figure 3a) and O₃ concentrations (Figure 3b) in Africa. The LC and NDVI are identified as the strongest positive drivers of isoprene emissions. This is consistent with the physics that biogenic isoprene is emitted mainly from terrestrial vegetation, and its emissions are directly influenced by LC types and the associated plant species. Among all meteorological variables, air temperature plays a dominate role in regulating isoprene emissions, exhibiting a positive correlation, in line with prior work (e.g., Singaas and Sharkey, 1998). For O₃ concentrations, meteorological factors – relative humidity, air temperature, precipitation, cloud cover, and incoming solar radiation – exert substantial influence, with temperature and solar radiation positively associated with O₃ levels. Additionally, precursor emissions constitute a vital component in O₃ formation. The VOCs-to-NO_x emission ratio, used here as an indicator of O₃ production regime in this study, is also a critical determinant of projected O₃.



350 **3.2 Climate-driven changes in biogenic isoprene emissions**

351 The projected changes in RF-predicted isoprene emissions over Africa in
352 2050 (averaged over 2050–2054) relative to 2020 (averaged over 2020–2024)
353 are shown in Figure 4. The isoprene emissions show increasing trends under
354 all four future scenarios. Shaped by the land cover characteristics in Africa,
355 there is a distinct north-south spatial distribution pattern in the changes in
356 isoprene emissions. Central Africa, as a major source of isoprene emissions,
357 exhibits the largest increases in biogenic isoprene emissions across Africa, with
358 a maximum growth rate exceeding $1.0 \text{ g/m}^2/\text{yr}$ under four scenarios. In contrast,
359 the land use type in Northern Africa is dominated by barren land, resulting in
360 consistently low isoprene emission levels. Compared to the period of 2020–
361 2024, the projected changes of isoprene in Northern Africa for 2050–2054 are
362 less than $0.1 \text{ g/m}^2/\text{yr}$, while the isoprene emissions increase by $0.1\text{--}0.5 \text{ g/m}^2/\text{yr}$
363 over Southern Africa under all SSPs.

364 According to the feature contributions derived by SHAP analysis, biogenic
365 isoprene emissions largely depend on meteorological fields, with air
366 temperature (at 2m) identified as the most critical factor (Figure 3a). A
367 comparison of future meteorological variables between 2050–2054 and 2020–
368 2024 under different scenarios demonstrates that near-surface air
369 temperatures elevate throughout the entire African continent in 2050–2054,
370 with SSP5-8.5 presenting the strongest warming (Figure 5). Therefore,
371 isoprene emission rates are anticipated to rise, especially in the strong warming



372 scenarios (i.e. SSP3-7.0 and SSP5-8.5). Besides, isoprene emissions show
373 opposite responses to humid weather conditions and the enhancement of
374 projected isoprene emissions induced by drought stress is particularly
375 pronounced over Central and Southern Africa (Figure 6).

376 Figure S1 shows the spatial distributions of biogenic isoprene emission
377 changes during 2050–2054 compared to 2020–2024 in March–April–May
378 (MAM), June–July–August (JJA), September–October–November (SON), and
379 December–January–February (DJF) under the four scenarios. The changes in
380 isoprene emissions do not show obvious seasonality, but there are relatively
381 larger increases in MAM and DJF than other seasons.

382 **3.3 Climate-driven changes in future O₃ concentrations over Africa**

383 Figure 7a shows the changes in annual mean near-surface O₃
384 concentrations in response to climate change under different scenarios, as
385 projected by the RF model using future meteorological fields from 18 CMIP6
386 models (O₃_MET). The projected O₃ exhibits an overall increasing trend during
387 2050–2054 relative to 2020–2024, indicating a climate penalty on air quality
388 over most African regions. Future increases in air temperature (Figure 5), along
389 with reductions in relative humidity (Figure 6) and cloud cover (Figure 8) will
390 enhance photochemical O₃ production, leading to substantial increases in O₃
391 levels, with maximum increases over 1.0 ppb, even reaching 2.0 ppb, under
392 strong warming scenarios. Under the weak warming scenario SSP1-2.6, the
393 climate-driven O₃ increases are relatively small, with increases of less than 1.0



394 ppb across Africa.

395 The ratio of VOCs-to-NO_x emissions is adopted to express the nonlinearity
396 of O₃ formation to its precursor emissions. Previous studies have revealed that
397 the O₃ formation regime in Africa is generally NO_x-limited (Ziemke et al., 2009;
398 Bela et al., 2015). Figure S2 shows that the ratio of VOCs-to-NO_x emissions
399 does not change from present-day to the mid-21st century, which demonstrates
400 that future O₃ production is also NO_x-sensitive over Africa. In NO_x-limited
401 regions, increases in biogenic isoprene emissions result in a slight decrease in
402 O₃ levels by less than 0.5 ppb over Central and Western Africa in 2050 relative
403 to 2020 (Figure 7b, O₃_NAT). The total effects of changing meteorological
404 factors and biogenic isoprene emissions on O₃ variations are similar to that due
405 to the changes in meteorological factors alone, as depicted in Figure 7c
406 (O₃_ALL). In summary, the climate-driven changes in meteorological
407 parameters exert a more dominant role in regulating future O₃ concentrations
408 over Africa through changing physical and chemical processes, while the
409 changing biogenic isoprene emissions exerts a minor role.

410 Climatology of meteorological fields over Africa has obvious seasonal
411 characteristics, and the formation of near-surface O₃ is tightly coupled with
412 climate-driven processes. Figures S3–S6 show the spatial distribution changes
413 in seasonal O₃ concentrations influenced by meteorological fields and biogenic
414 isoprene emissions under climate change. O₃ concentration increases the most
415 during MAM, with a maximum rise reaching up to 3.8 ppb over Central and



416 Southern Africa under the SSP5-8.5 scenario (Figure S3). In contrast, parts of
417 Southern Africa show a reduction of 0.2–1.0 ppb during SON under all
418 scenarios (Figure S5), primarily related to a higher sea level pressure (Figure
419 S7) and its negative correlation with O₃ levels (Figure 3b). Additionally, a
420 decrease exceeding 0.5 ppb is expected across Central Africa in DJF under the
421 strong warming scenarios (Figure S6), largely driven by the rapid increases in
422 precipitation frequency (Figure S8). Moreover, increasing isoprene emissions
423 also contribute to the decrease in O₃ concentrations by 0.2–0.5 ppb over
424 Eastern and Central Africa during JJA (Figure S4).

425 **3.4 Projection of mortality attributed to O₃ and temperature**

426 Figure 9 shows the relative changes in future projected mortality burden in
427 2050 compared to that in 2020 corresponding to changes in O₃ concentrations
428 and air temperatures across Africa under the four future scenarios. The
429 mortality due to the changes in O₃ pollution driven by changes in meteorological
430 factors and biogenic isoprene emissions are separately investigated. It is worth
431 noting that the potential amplification or suppression effects of interactions
432 between O₃ and temperature on mortality are not considered in this study.

433 Mortality ratios (MRs) over Africa are presented in 2050 relative to 2020,
434 with temperature-related MRs (MR_{temperature}) increases much higher than those
435 due to the climate-driven increases in O₃ exposure levels (MR_{ozone}), particularly
436 under the SSP3-7.0 and SSP5-8.5 scenarios. This demonstrates that increases
437 in extreme heat in a warmer future are projected to cause substantially more



438 deaths than the climate-driven increases in extreme O₃ concentrations across
439 Africa. The MR_{temperature} ranges from 1.007 to 1.015, with an average of 1.0115.
440 The MRs due to climate-driven O₃ changes related to the meteorological
441 parameters (MR_{ozone-met}) show a slight increase from 1.0002 to 1.0006, as the
442 climate getting warmer. In contrast, MRs attributed to climate-driven O₃
443 changes related to biogenic isoprene emissions (MR_{ozone-nat}) do not show any
444 noticeable change under different scenarios, which exceed 1.0 only under the
445 SSP3-7.0 scenario. Nevertheless, these suggest that environmental conditions
446 for human health in Africa will be deteriorated in a warming climate with more
447 frequent extreme heat together with intensified O₃ pollution.

448 **4. Conclusion and discussions**

449 Africa is a vast continent with a population accounting for more than one-
450 eighth of total population in the world. In the process of rapid urbanization,
451 industrialization, and motorization, the O₃ pollution across the continent has
452 been exacerbating, which poses a serious threat to the public health. In this
453 study, we predict future near-surface O₃ concentrations over Africa from 2020
454 to 2050 driven by climate change under four different scenarios (SSP1-2.6,
455 SSP2-4.5, SSP3-7.0, and SSP5-8.5) based on an interpretable RF model
456 integrated with multi-source data, such as GEOS-Chem model simulations,
457 future meteorological fields from CMIP6 multi-model outputs, O₃ precursor
458 emissions, topography, land use, population density, and spatiotemporal
459 information.



460 Biogenic isoprene emissions are strongly influenced by land use and
461 climate change, which in turn modulate O₃ concentrations through atmospheric
462 photochemical reactions. With rising air temperatures, the RF model-projected
463 biogenic isoprene emissions across Africa are expected to increase in 2050
464 relative to 2020 under future climate scenarios. Owing to distinctive
465 characteristics of vegetation coverage and composition, the most substantial
466 increase of isoprene emissions occurs over Central Africa, where the maximum
467 increase is projected to exceed 1.0 g/m²/yr under the SSP2-4.5, SSP3-7.0, and
468 SSP5-8.5 scenarios. In contrast, the isoprene emissions in Northern Africa
469 show minimal variabilities.

470 The impacts of biogenic isoprene emissions and meteorological fields
471 under future climate change on O₃ levels across Africa are separately quantified.
472 In general, climate change has the potential to increase O₃ concentrations,
473 known as the “O₃ climate penalty”. Favorable meteorological conditions such
474 as higher temperature and lower relative humidity facilitate the photochemical
475 generation of O₃, with a maximum increase of 2.0 ppb in 2050 compared to
476 2020. In this NO_x-limited region, the simultaneously increased biogenic
477 isoprene emissions lead to a slight O₃ decline (<0.5 ppb). Meteorological fields
478 play a dominant role in shaping future O₃ levels over Africa than biogenic
479 isoprene emissions. In addition, the low-emission scenarios (SSP1-2.6 and
480 SSP2-4.5) are projected to prompt less increases in O₃ levels than the high-
481 emission scenarios (SSP3-7.0 and SSP5-8.5). This study reveals that global



482 warming will exacerbate the health risk associated with O₃ pollution across
483 Africa. It further highlights that elevated air temperatures act as the primary
484 driver of increased mortality ratios in Africa, while enhanced O₃ concentrations
485 is an additional stressor as an adverse side effect of warming climate.

486 To assess the role of climate change in future O₃ variations, O₃
487 concentrations from the CMIP6 multi-model future predictions are obtained,
488 which are driven by changes in anthropogenic emissions, climate and land use
489 following SSPs scenarios. The spatial distributions of simulated differences in
490 O₃ concentration over Africa between 2020 and 2050 are shown in Figure 10.
491 Under the SSP1-2.6 and SSP2-4.5 scenarios, O₃ concentrations are predicted
492 to decrease by less than 10 ppb, mainly resulting from reductions in
493 anthropogenic emissions. However, O₃ concentrations are expected to increase
494 under the SSP3-7.0 and SSP5-8.5 scenarios, with the rise up to 1–5 ppb across
495 Africa, which are largely contributed by the climate change in a warming future.

496 In this study, the O₃ projections over Africa are subject to uncertainties and
497 limitations arising from input datasets, GEOS-Chem model simulations, CMIP6
498 multi-model simulations of meteorology, and the RF model. First, land use,
499 topography and population density data are held at present-day values when
500 predicting future O₃ concentrations; these factors will change with climate and
501 may bias projections. Second, the RF model training and performance strongly
502 relies on the accuracy of GEOS-Chem simulation results. Although the GEOS-
503 Chem model has been proven capable of capturing the temporal and spatial



504 variations of global O_3 , there remain certain uncertainties in its simulated O_3
505 concentrations over Africa. These uncertainties mainly stem from discrepancies
506 in emission inventories, including anthropogenic, biogenic, biomass burning,
507 and lightning sources (Han et al., 2018). Third, the CMIP6 multi-model
508 meteorological fields used to represent future climate under different scenarios
509 may suffer projection uncertainties and can introduce biases (Xu et al., 2021).
510 Fourth, the contributions of selected features in this study reflect the aggregate
511 study domain; future work should train region-specific RF models to estimate
512 near-surface O_3 concentrations and quantify variable contributions at regional
513 scales. Finally, dependencies among the RF model input features can confound
514 attribution, which may potentially result in spurious interpretations (Silva and
515 Keller, 2024). Furthermore, when quantifying future O_3 changes driven by
516 biogenic emissions, only biogenic isoprene emissions are considered, which
517 may have led to a low bias of the influence from biogenic emissions.



518 ***Author contributions***

519 HL and YY designed the research. HL performed the model simulations,
520 analyzed data and wrote the initial draft. YY and HW helped edit and review the
521 manuscript. All the authors discussed the results and contributed to the final
522 manuscript.

523 ***Code and data availability***

524 The GEOS-Chem model is available at <https://zenodo.org/records/7254273>.
525 MERRA-2 reanalysis data can be downloaded at
526 <https://gmao.gsfc.nasa.gov/reanalysis/MERRA-2/>. Multi-model projections of
527 climate variables are from Scenario Model Intercomparison Project in Phase 6
528 of the Coupled Model Intercomparison Project [https://esgf-](https://esgf-node.llnl.gov/search/cmip6/)
529 [node.llnl.gov/search/cmip6/](https://esgf-node.llnl.gov/search/cmip6/). Land cover is derived from
530 <http://maps.elie.ucl.ac.be/CCI/viewer/download.php>. Normalized difference
531 vegetation index is obtained from [https://www.ncei.noaa.gov/data/land-](https://www.ncei.noaa.gov/data/land-normalized-difference-vegetation-index/access/)
532 [normalized-difference-vegetation-index/access/](https://www.ncei.noaa.gov/data/land-normalized-difference-vegetation-index/access/). Topography is collected from
533 <https://cgiarcsi.community/data/srtm-90m-digital-elevation-database-v4-1/>.
534 Population density is acquired from [https://landscan.ornl.gov/landscan-](https://landscan.ornl.gov/landscan-datasets)
535 [datasets](https://landscan.ornl.gov/landscan-datasets).

536 ***Acknowledgments***

537 The Pacific Northwest National Laboratory (PNNL) is operated for DOE by the
538 Battelle Memorial Institute under contract DE-AC05-76RLO1830.

539 ***Financial support***



540 This study was supported by the National Natural Science Foundation of China
541 (Grants 42505179 and 42475032), and Jiangsu Innovation and
542 Entrepreneurship Team (Grant JSSCTD202346).

543 ***Competing Interest***

544 At least one of the (co-)authors is a member of the editorial board of
545 Atmospheric Chemistry and Physics. The authors also have no other competing
546 interests to declare..



547 **References**

- 548 Anenberg, S. C., Horowitz, L. W., Tong, D. Q., and West, J. J.: An estimate of
 549 the global burden of anthropogenic ozone and fine particulate matter on
 550 premature human mortality using atmospheric modeling, *Environ. Health*
 551 *Perspect.*, 118, 1189–1195, <https://doi.org/10.1289/ehp.0901220>, 2010.
- 552
- 553 Ban, J., Lu, K., Wang, Q., and Li, T.: Climate change will amplify the inequitable
 554 exposure to compound heatwave and ozone pollution, *One Earth*, 5, 677–686,
 555 <https://doi.org/10.1016/j.oneear.2022.05.007>, 2022.
- 556
- 557 Bela, M. M., Longo, K. M., Freitas, S. R., Moreira, D. S., Beck, V., Wofsy, S. C.,
 558 Gerbig, C., Wiedemann, K., Andreae, M. O., and Artaxo, P.: Ozone production
 559 and transport over the Amazon Basin during the dry-to-wet and wet-to-dry
 560 transition seasons, *Atmos. Chem. Phys.*, 15, 757–782,
 561 <https://doi.org/10.5194/acp-15-757-2015>, 2015.
- 562
- 563 Bey, I., Jacob, D. J., Yantosca, R. M., Logan, J. A., Field, B. D., Fiore, A. M., Li,
 564 Q., Liu, H. Y., Mickley, L. J., and Schultz, M. G.: Global modeling of tropospheric
 565 chemistry with assimilated meteorology: Model description and evaluation, *J.*
 566 *Geophys. Res. Atmos.*, 106, 23073–23095,
 567 <https://doi.org/10.1029/2001JD000807>, 2001.
- 568
- 569 Breiman, L.: Random forests, *Mach. Learn.*, 45, 5–32,
 570 <https://doi.org/10.1023/a:1010933404324>, 2001.
- 571
- 572 Brown, F., Folberth, G. A., Sitch, S., Bauer, S., Bauters, M., Boeckx, P.,
 573 Cheesman, A. W., Deushi, M., Dos Santos Vieira, I., Galy-Lacaux, C., Haywood,
 574 J., Keeble, J., Mercado, L. M., O'Connor, F. M., Oshima, N., Tsigaridis, K., and
 575 Verbeek, H.: The ozone-climate penalty over South America and Africa by
 576 2100, *Atmos. Chem. Phys.*, 22, 12331–12352, [https://doi.org/10.5194/acp-22-](https://doi.org/10.5194/acp-22-12331-2022)
 577 [12331-2022](https://doi.org/10.5194/acp-22-12331-2022), 2022.
- 578
- 579 Colette, A., Andersson, C., Baklanov, A., Bessagnet, B., Brandt, J., Christensen,
 580 J. H., Doherty, R., Engardt, M., Geels, C., Giannakopoulos, C., Hedegaard, G.
 581 B., Katragkou, E., Langner, J., Lei, H., Manders, A., Melas, D., Meleux, F., Rouïl,
 582 L., Sofiev, M., Soares, J., Stevenson, D. S., Tombrou-Tzella, M., Varotsos, K.
 583 V., and Young, P.: Is the ozone climate penalty robust in Europe? *Environ. Res.*
 584 *Lett.*, 10, 084015, <https://doi.org/10.1088/1748-9326/10/8/084015>, 2015.
- 585
- 586 Colombi, N., Miyazaki, K., Bowman, K. W., Neu, J. L., and Jacob, D. J.: A new
 587 methodology for inferring surface ozone from multispectral satellite
 588 measurements, *Environ. Res. Lett.*, 16, 105005, [https://doi.org/10.1088/1748-](https://doi.org/10.1088/1748-9326/ac243d)
 589 [9326/ac243d](https://doi.org/10.1088/1748-9326/ac243d), 2021.



- 590
 591 Cromar, K. R., Anenberg, S. C., Balmes, J. R., Fawcett, A. A., Ghazipura, M.,
 592 Gohlke, J. M., Hashizume, M., Howard, P., Lavigne, E., Levy, K., Madrigano,
 593 J., Martinich, J. A., Mordecai, E. A., Rice, M. B., Saha, S., Scovronick, N. C.,
 594 Sekercioglu, F., Svendsen, E. R., Zaitchik, B. F., and Ewart, G.: Global Health
 595 Impacts for Economic Models of Climate Change: A Systematic Review and
 596 Meta-Analysis, *Ann. Am. Thorac. Soc.*, 19, 1203–1212,
 597 <https://doi.org/10.1513/AnnalsATS.202110-1193OC>, 2022.
 598
 599 Doherty, R. M., Wild, O., Shindell, D. T., Zeng, G., MacKenzie, I. A., Collins, W.
 600 J., Fiore, A. M., Stevenson, D. S., Dentener, F. J., Schultz, M. G., Hess, P.,
 601 Derwent, R. G., and Keating, T. J.: Impacts of climate change on surface ozone
 602 and intercontinental ozone pollution: A multi-model study, *J. Geophys. Res.*
 603 *Atmos.*, 118, 3744–3763, <https://doi.org/10.1002/jgrd.50266>, 2013.
 604
 605 Fajersztajn, L., Veras, M., Barrozo, L. V., and Saldiva, P.: Air monitoring
 606 coverage in low-income countries: an observational study, *Lancet*, 384, S14,
 607 [https://doi.org/10.1016/s0140-6736\(14\)61877-8](https://doi.org/10.1016/s0140-6736(14)61877-8), 2014.
 608
 609 Fehsenfeld, F., Calvert, J., Fall, R., Goldan, P., Guenther, A. B., Hewitt, C. N.,
 610 Lamb, B., Liu, S., Trainer, M., Westberg, H., and Zimmerman, P.: Emissions of
 611 volatile organic compounds from vegetation and the implications for
 612 atmospheric chemistry, *Global Biogeochem. Cy.*, 6, 389–430,
 613 <https://doi.org/10.1029/92GB02125>, 1992.
 614
 615 Fisher, S., David, C., Bellinger, M. L., Cropper, P. K., Agnes, B., Juliette, B. K.,
 616 Yongjoon, P., Gabriella, T., and Philip, J. L.: Air pollution and development in
 617 Africa: Impacts on health, the economy, and human capital, *Lancet Planet.*
 618 *Health*, 5, e681–e688, [https://doi.org/10.1016/S2542-5196\(21\)00201-1](https://doi.org/10.1016/S2542-5196(21)00201-1), 2021.
 619
 620 Fu, T.-M., and Tian, H.: Climate change penalty to ozone air quality: Review of
 621 current understandings and knowledge gaps, *Curr. Pollut. Rep.*, 5, 159–171,
 622 <https://doi.org/10.1007/s40726-019-00115-6>, 2019.
 623
 624 Gao, J., Yang, Y., Wang, H., Wang, P., Li, H., Li, M., Ren, L., Yue, X., and Liao,
 625 H.: Fast climate responses to emission reductions in aerosol and ozone
 626 precursors in China during 2013–2017, *Atmos. Chem. Phys.*, 22, 7131–7142,
 627 <https://doi.org/10.5194/acp-22-7131-2022>, 2022.
 628
 629 Gaudel, A., Cooper, O. R., Ancellet, G., Barret, B., Boynard, A., Burrows, J. P.,
 630 Clerbaux, C., Coheur, P. F., Cuesta, J., Cuevas, E., Doniki, S., Dufour, G.,
 631 Ebojie, F., Foret, G., Garcia, O., Granados-Muñoz, M. J., Hannigan, J. W., Hase,
 632 F., Hassler, B., Huang, G., Hurtmans, D., Jaffe, D., Jones, N., Kalabokas, P.,
 633 Kerridge, B., Kulawik, S., Latter, B., Leblanc, T., Le Flochmoën, E., Lin, W., Liu,



634 J., Liu, X., Mahieu, E., McClure-Begley, A., Neu, J. L., Osman, M., Palm, M.,
 635 Petetin, H., Petropavlovskikh, I., Querel, R., Rahpoe, N., Rozanov, A., Schultz,
 636 M. G., Schwab, J., Siddans, R., Smale, D., Steinbacher, M., Tanimoto, H.,
 637 Tarasick, D. W., Thouret, V., Thompson, A. M., Trickl, T., Weatherhead, E.,
 638 Wespes, C., Worden, H. M., Vigouroux, C., Xu, X., Zeng, G., and Ziemke, J.:
 639 Tropospheric Ozone Assessment Report: Present-day distribution and trends
 640 of tropospheric ozone relevant to climate and global atmospheric chemistry
 641 model evaluation, *Elem. Sci. Anth.*, 6, 39, <https://doi.org/10.1525/elementa.291>,
 642 2018.

643
 644 GBD 2019 Risk Factors Collaborators: Global burden of 87 risk factors in 204
 645 countries and territories, 1990–2019: a systematic analysis for the Global
 646 Burden of Disease Study 2019, *Lancet*, 396, 1223–1249,
 647 [https://doi.org/10.1016/S0140-6736\(20\)30752-2](https://doi.org/10.1016/S0140-6736(20)30752-2), 2020.

648
 649 Gelaro, R., McCarty, W., Suárez, M. J., Todling, R., Molod, A., Takacs, L.,
 650 Randles, C. A., Darmenov, A., Bosilovich, M. G., Reichle, R., Wargan, K., Coy,
 651 L., Cullather, R., Draper, C., Akella, S., Buchard, V., Conaty, A., da Silva, A. M.,
 652 Gu, W., Kim, G.-K., Koster, R., Lucchesi, R., Merkova, D., Nielsen, J. E.,
 653 Partyka, G., Pawson, S., Putman, W., Rienecker, M., Schubert, S. D.,
 654 Sienkiewicz, M., and Zhao, B.: The Modern-Era Retrospective Analysis for
 655 Research and Applications, Version 2 (MERRA-2), *J. Clim.*, 30, 5419–5454,
 656 <https://doi.org/10.1175/JCLI-D-16-0758.1>, 2017.

657
 658 Gong, C., and Liao, H.: A typical weather pattern for ozone pollution events in
 659 North China, *Atmos. Chem. Phys.*, 19, 13725–13740,
 660 <https://doi.org/10.5194/acp-19-13725-2019>, 2019.

661
 662 Guenther, A., Hewitt, C. N., Erickson, D., Fall, R., Geron, C., Graedel, T., Harley,
 663 P., Klinger, L., Lerdau, M., Mckay, W. A., Pierce, T., Scholes, B., Steinbrecher,
 664 R., Tallamraju, R., Taylor, J., and Zimmerman, P.: A global model of natural
 665 volatile organic compound emissions, *J. Geophys. Res. Atmos.*, 100, 8873–
 666 8892, <https://doi.org/10.1029/94jd02950>, 1995.

667
 668 Guenther, A. B., Jiang, X., Heald, C. L., Sakulyanontvittaya, T., Duhl, T.,
 669 Emmons, L. K., and Wang, X.: The Model of Emissions of Gases and Aerosols
 670 from Nature version 2.1 (MEGAN2.1): an extended and updated framework for
 671 modeling biogenic emissions, *Geosci. Model Dev.*, 5, 1471–1492,
 672 <https://doi.org/10.5194/gmd-5-1471-2012>, 2012.

673
 674 Han, H., Liu, J., Yuan, H., Zhuang, B., Zhu, Y., Wu, Y., Yan, Y., and Ding, A.:
 675 Characteristics of intercontinental transport of tropospheric ozone from Africa
 676 to Asia, *Atmos. Chem. Phys.*, 18, 4251–4276, <https://doi.org/10.5194/acp-18-4251-2018>, 2018.

677



678
 679 Hou, L., Dai, Q., Song, C., Liu, B., Guo, F., Dai, T., Li, L., Liu, B., Bi, X., Zhang,
 680 Y., and Feng, Y.: Revealing Drivers of Haze Pollution by Explainable Machine
 681 Learning, *Environ. Sci. Technol. Lett.*, 9, 112–119,
 682 <https://doi.org/10.1021/acs.estlett.1c00865>, 2022.
 683
 684 Hudman, R. C., Moore, N. E., Mebust, A. K., Martin, R. V., Russell, A. R., Valin,
 685 L. C., and Cohen, R. C.: Steps towards a mechanistic model of global soil nitric
 686 oxide emissions: implementation and space based-constraints, *Atmos. Chem.*
 687 *Phys.*, 12, 7779–7795, <https://doi.org/10.5194/acp-12-7779-2012>, 2012.
 688
 689 IPCC: Climate change 2021: The physical science basis. Contribution of
 690 working group I to the sixth assessment report of the intergovernmental panel
 691 on climate change, Cambridge, UK, Cambridge University Press,
 692 <https://doi.org/10.1017/9781009157896>, 2021.
 693
 694 Iyakaremye, V., Zeng, G., Yang, X., Zhang, G., Ullah, I., Gahigi, A., Vuguziga,
 695 F., Asfaw, T. G., and Ayugi, B.: Increased high-temperature extremes and
 696 associated population exposure in Africa by the mid-21st century, *Sci. Total*
 697 *Environ.*, 790, 148162, <https://doi.org/10.1016/j.scitotenv.2021.148162>, 2021.
 698
 699 Jaars, K., van Zyl, P. G., Beukes, J. P., Hellén, H., Vakkari, V., Josipovic, M.,
 700 Venter, A. D., Räsänen, M., Knoetze, L., Cilliers, D. P., Siebert, S. J., Kulmala,
 701 M., Rinne, J., Guenther, A., Laakso, L., and Hakola, H.: Measurements of
 702 biogenic volatile organic compounds at a grazed savannah grassland
 703 agricultural landscape in South Africa, *Atmos. Chem. Phys.*, 16, 15665–15688,
 704 <https://doi.org/10.5194/acp-16-15665-2016>, 2016.
 705
 706 Jacob, D. J., and Winner, D. A.: Effect of climate change on air quality, *Atmos.*
 707 *Environ.*, 43, 51–63, <https://doi.org/10.1016/j.atmosenv.2008.09.051>, 2009.
 708
 709 Kavassalis, S. C., and Murphy, J. G.: Understanding ozone-meteorology
 710 correlations: A role for dry deposition, *Geophys. Res. Lett.*, 44, 2922–2931,
 711 <https://doi.org/10.1002/2016gl071791>, 2017.
 712
 713 Kesselmeier, J., and Staudt, M.: Biogenic volatile organic compounds (VOC):
 714 An overview on emission, physiology and ecology, *J. Atmos. Chem.*, 33, 23–
 715 88, <https://doi.org/10.1023/A:1006127516791>, 1999.
 716
 717 Lee, J. Y., and Kim, H.: Projection of future temperature-related mortality due
 718 to climate and demographic changes, *Environ. Int.*,
 719 <http://dx.doi.org/10.1016/j.envint.2016.06.007>, 2016.
 720



- 721 Lelieveld, J., Evans, J. S., Fnais, M., Giannadaki, D., and Pozzer, A.: The
 722 contribution of outdoor air pollution sources to premature mortality on a global
 723 scale, *Nature*, 525, 367–371, <https://doi.org/10.1038/nature15371>, 2015.
 724
- 725 Li, H., Yang, Y., Wang, H., Wang, P., Yue, X., and Liao, H.: Projected Aerosol
 726 Changes Driven by Emissions and Climate Change Using a Machine Learning
 727 Method, *Environ. Sci. Technol.*, 56, 3884–3893,
 728 <https://doi.org/10.1021/acs.est.1c04380>, 2022.
 729
- 730 Li, H., Yang, Y., Jin, J., Wang, H., Li, K., Wang, P., and Liao, H.: Climate driven
 731 deterioration of future ozone pollution in Asia predicted by machine learning
 732 with multi-source data, *Atmos. Chem. Phys.*, 23, 1131–1145,
 733 <https://doi.org/10.5194/acp-23-1131-2023>, 2023.
 734
- 735 Li, H., Yang, Y., Su, H., Wang, H., Wang, P., and Liao, H.: Ozone pollution in
 736 China affected by climate change in a carbon neutral future as predicted by a
 737 process-based interpretable machine learning method, *Geophys. Res. Lett.*, 51,
 738 e2024GL109520, <https://doi.org/10.1029/2024GL109520>, 2024.
 739
- 740 Lin, J.-T., and McElroy, M. B.: Impacts of boundary layer mixing on pollutant
 741 vertical profiles in the lower troposphere: Implications to satellite remote
 742 sensing, *Atmos. Environ.*, 44, 1726–1739,
 743 <https://doi.org/10.1016/j.atmosenv.2010.02.009>, 2010.
 744
- 745 Liu, X., Zhu, Y., Xue, L., Desai, A. R., and Wang, H.: Cluster-enhanced
 746 ensemble learning for mapping global monthly surface ozone from 2003 to
 747 2019, *Geophys. Res. Lett.*, 49, e2022GL097947,
 748 <https://doi.org/10.1029/2022GL097947>, 2022.
 749
- 750 Liu, Y., Schallhart, S., Taipale, D., Tykkä, T., Räsänen, M., Merbold, L., Hellén,
 751 H., and Pellikka, P.: Seasonal and diurnal variations in biogenic volatile organic
 752 compounds in highland and lowland ecosystems in southern Kenya, *Atmos.*
 753 *Chem. Phys.*, 21, 14761–14787, <https://doi.org/10.5194/acp-21-14761-2021>,
 754 2021.
 755
- 756 Liu, Z., Doherty, R. M., Wild, O., O'Connor, F. M., and Turnock, S. T.: Correcting
 757 ozone biases in a global chemistry–climate model: implications for future ozone,
 758 *Atmos. Chem. Phys.*, 22, 12543–12557, [https://doi.org/10.5194/acp-22-12543-](https://doi.org/10.5194/acp-22-12543-2022)
 759 2022, 2022.
 760
- 761 Lu, X., Zhang, L., and Shen, L.: Meteorology and climate influences on
 762 tropospheric ozone: A Review of natural sources, chemistry, and transport
 763 patterns, *Curr. Pollut. Rep.*, 5, 238–260, [https://doi.org/10.1007/s40726-019-](https://doi.org/10.1007/s40726-019-00118-3)
 764 00118-3, 2019.



765
 766 Lundberg, S. M., and Lee, S.-I.: A unified approach to interpreting model
 767 predictions, *Adv. Neural Inf. Process. Syst.*, 30, 4768–4777,
 768 <https://doi.org/10.48550/arXiv.1705.07874>, 2017.
 769
 770 Lyu, X., Li, K., Guo, H., Morawska, L., Zhou, B., Zeren, Y., Jiang, F., Chen, C.,
 771 Goldstein, A. H., Xu, X., Wang, T., Lu, X., Zhu, T., Querol, X., Chatani, S., Latif,
 772 M. T., Schuch, D., Sinha, V., Kumar, P., Mullins, B., Seguel, R., Shao, M., Xue,
 773 L., Wang, N., Chen, J., Gao, J., Chai, F., Simpson, I., Sinha, B., and Blake, D.
 774 R.: A synergistic ozone-climate control to address emerging ozone pollution
 775 challenges, *One Earth*, 6, 964–977,
 776 <https://doi.org/10.1016/j.oneear.2023.07.004>, 2023.
 777
 778 Malashock, D. A., Delang, M. N., Becker, J. S., Serre, M. L., West, J. J., Chang,
 779 K. L., Cooper, O. R., and Anenberg, S. C.: Global trends in ozone concentration
 780 and attributable mortality for urban, peri-urban, and rural areas between 2000
 781 and 2019: a modelling study, *Lancet Planet. Health*, 6, e958–e967,
 782 [https://doi.org/10.1016/S2542-5196\(22\)00260-1](https://doi.org/10.1016/S2542-5196(22)00260-1), 2022.
 783
 784 Mao, J., Paulot, F., Jacob, D. J., Cohen, R. C., Crounse, J. D., Wennberg, P.
 785 O., Keller, C. A., Hudman, R. C., Barkley, M. P., and Horowitz, L. W.: Ozone
 786 and organic nitrates over the eastern United States: sensitivity to isoprene
 787 chemistry, *J. Geophys. Res. Atmos.*, 118, 11256–68,
 788 <https://doi.org/10.1002/jgrd.50817>, 2013.
 789
 790 Marais, E. A., Jacob, D. J., Kurosu, T. P., Chance, K., Murphy, J. G., Reeves,
 791 C., Mills, G., Casadio, S., Millet, D. B., Barkley, M. P., Paulot, F., and Mao, J.:
 792 Isoprene emissions in Africa inferred from OMI observations of formaldehyde
 793 columns, *Atmos. Chem. Phys.*, 12, 6219–6235, <https://doi.org/10.5194/acp-12-6219-2012>, 2012.
 794
 795 McLinden, C. A., Olsen, S. C., Hannegan, B., Wild, O., Prather, M. J., and
 796 Sundet, J.: Stratospheric ozone in 3-D models: A simple chemistry and the
 797 cross-tropopause flux, *J. Geophys. Res. Atmos.*, 105, 14653–14665,
 798 <https://doi.org/10.1029/2000jd900124>, 2000.
 800
 801 Murray, L. T., Jacob, D. J., Logan, J. A., Hudman, R. C., and Koshak, W. J.:
 802 Optimized regional and interannual variability of lightning in a global chemical
 803 transport model constrained by LIS/OTD satellite data, *J. Geophys. Res.*
 804 *Atmos.*, 117, D20307, <https://doi.org/10.1029/2012jd017934>, 2012.
 805
 806 Murray, L. T.: Lightning NO_x and Impacts on Air Quality, *Curr. Pollut. Rep.*, 2,
 807 115–133, <https://doi.org/10.1007/s40726-016-0031-7>, 2016.
 808



- 809 Mills, G., Pleijel, H., Malley, C. S., Sinha, B., Cooper, O. R., Schultz, M. G.,
 810 Neufeld, H. S., Simpson, D., Sharps, K., Feng, Z., Gerosa, G., Harmens, H.,
 811 Kobayashi, K., Saxena, P., Paoletti, E., Sinha, V., and Xu, X.: Tropospheric
 812 ozone assessment report: Present-day tropospheric ozone distribution and
 813 trends relevant to vegetation, *Elem. Sci. Anth.*, 6, 47,
 814 <https://doi.org/10.1525/elementa.302>, 2018.
- 815
 816 Myhre, G., Aas, W., Cherian, R., Collins, W., Faluvegi, G., Flanner, M., Forster,
 817 P., Hodnebrog, Ø., Klimont, Z., Lund, M. T., Mülmenstädt, J., Lund Myhre, C.,
 818 Olivé, D., Prather, M., Quaas, J., Samset, B. H., Schnell, J. L., Schulz, M.,
 819 Shindell, D., Skeie, R. B., Takemura, T., and Tsyro, S.: Multi-model simulations
 820 of aerosol and ozone radiative forcing due to anthropogenic emission changes
 821 during the period 1990–2015, *Atmos. Chem. Phys.*, 17, 2709–2720,
 822 <https://doi.org/10.5194/acp-17-2709-2017>, 2017.
- 823
 824 Ni, Y., Yang, Y., Wang, H., Li, H., Li, M., Wang, P., Li, K., and Liao, H.:
 825 Contrasting changes in ozone during 2019–2021 between eastern and the
 826 other regions of China attributed to anthropogenic emissions and
 827 meteorological conditions, *Sci. Total Environ.*, 908, 168272,
 828 <https://doi.org/10.1016/j.scitotenv.2023.168272>, 2024.
- 829
 830 O'Neill, B. C., Tebaldi, C., van Vuuren, D. P., Eyring, V., Friedlingstein, P., Hurtt,
 831 G., Knutti, R., Kriegler, E., Lamarque, J.-F., Lowe, J., Meehl, G. A., Moss, R.,
 832 Riahi, K., and Sanderson, B. M.: The Scenario Model Intercomparison Project
 833 (ScenarioMIP) for CMIP6, *Geosci. Model Dev.*, 9, 3461–3482,
 834 <https://doi.org/10.5194/gmd-9-3461-2016>, 2016.
- 835
 836 O'Rourke, P., Smith, S., Mott, A., Ahsan, H., McDuffie, E., and Crippa, M.:
 837 CEDS v_2021_04_21 Gridded emissions data,
 838 <https://doi.org/10.25584/PNNLDATAHUB/1779095>, 2021.
- 839
 840 Ott, L. E., Pickering, K. E., Stenchikov, G. L., Allen, D. J., DeCaria, A. J., Ridley,
 841 B., Lin, R.-F., Lang, S., and Tao, W.-K.: Production of lightning NO_x and its
 842 vertical distribution calculated from three-dimensional cloud-scale chemical
 843 transport model simulations, *J. Geophys. Res. Atmos.*, 115, D04301,
 844 <https://doi.org/10.1029/2009JD011880>, 2010.
- 845
 846 Park, R. J., Jacob, D. J., Field, B. D., Yantosca, R. M., and Chin, M.: Natural
 847 and transboundary pollution influences on sulfate-nitrate-ammonium aerosols
 848 in the United States: Implications for policy, *J. Geophys. Res. Atmos.*, 109, 20,
 849 <https://doi.org/10.1029/2003jd004473>, 2004.
- 850
 851 Pye, H. O. T., Liao, H., Wu, S., Mickley, L. J., Jacob, D. J., Henze, D. K., and
 852 Seinfeld, J. H.: Effect of changes in climate and emissions on future sulfate-



- 853 nitrate-ammonium aerosol levels in the United States, *J. Geophys. Res. Atmos.*,
 854 114, D01205, <https://doi.org/10.1029/2008jd010701>, 2009.
- 855
- 856 Requia, W. J., Di, Q., Silvern, R., Kelly, J. T., Koutrakis, P., Mickley, L. J.,
 857 Sulprizio, M. P., Amini, H., Shi, L., and Schwartz, J.: An ensemble learning
 858 approach for estimating high spatiotemporal resolution of ground level ozone in
 859 the contiguous United States, *Environ. Sci. Technol.*, 54, 11037–11047,
 860 <https://doi.org/10.1021/acs.est.0c01791>, 2020.
- 861
- 862 Rodriguez, J. D., Perez, A., and Lozano, J. A.: Sensitivity analysis of k-fold
 863 cross validation in prediction error estimation, *IEEE T. Pattern Anal.*, 32, 569–
 864 575, <https://doi.org/10.1109/TPAMI.2009.187>, 2010.
- 865
- 866 Sicard, P., Agathokleous, E., Anenberg, S. C., De Marco, A., Paoletti, E., and
 867 Calatayud, V.: Trends in urban air pollution over the last two decades: A global
 868 perspective, *Sci. Total Environ.*, 858, 160064,
 869 <https://doi.org/10.1016/j.scitotenv.2022.160064>, 2023.
- 870
- 871 Silva, S. J., and Keller, C. A.: Limitations of XAI methods for process-level
 872 understanding in the atmospheric sciences, *Artif. Intell. Earth Syst.*, 3, e230045,
 873 <https://doi.org/10.1175/AIES-D-23-0045.1>, 2024.
- 874
- 875 Sindelarova, K., Markova, J., Simpson, D., Huszar, P., Karlicky, J., Darras, S.,
 876 and Granier, C.: High-resolution biogenic global emission inventory for the time
 877 period 2000–2019 for air quality modelling, *Earth Syst. Sci. Data*, 14, 251–270,
 878 <https://doi.org/10.5194/essd-14-251-2022>, 2022.
- 879
- 880 Singaas, E. L., and Sharkey, T. D.: The regulation of isoprene emission
 881 responses to rapid leaf temperature fluctuations, *Plant Cell Environ.*, 21, 1181–
 882 1188, <https://doi.org/10.1046/j.1365-3040.1998.00380.x>, 1998.
- 883
- 884 Stirnberg, R., Cermak, J., Kotthaus, S., Haeffelin, M., Andersen, H., Fuchs, J.,
 885 Kim, M., Petit, J.-E., and Favez, O.: Meteorology-driven variability of air
 886 pollution (PM₁) revealed with explainable machine learning, *Atmos. Chem.*
 887 *Phys.*, 21, 3919–3948, <https://doi.org/10.5194/acp-21-3919-2021>, 2021.
- 888
- 889 Tobías, A., Hashizume, M., Honda, Y., Sera, F., Ng, C. F. S., Kim, Y., Roye, D.,
 890 Chung, Y., Dang, T. N., Kim, H., Lee, W., Íñiguez, C., Vicedo-Cabrera, A.,
 891 Abrutzky, R., Guo, Y., Tong, S., de Sousa Zanotti Stagliorio, M., Saldiva, P. H.
 892 N., Lavigne, E., Correa, P. M., Ortega, N. V., Kan, H., Osorio, S., Kyselý, J.,
 893 Urban, A., Orru, H., Indermitte, E., Jaakkola, J. J. K., Rytí, N. R. I., Pascal, M.,
 894 Huber, V., Schneider, A., Katsouyanni, K., Analitis, A., Entezari, A., Mayvaneh,
 895 F., Goodman, P., Zeka, A., Michelozzi, P., de'Donato, F., Alahmad, B., Diaz, M.
 896 H., De la Cruz Valencia, C., Overcenco, A., Houthuijs, D., Ameling, C., Rao, S.,



- 897 Di Ruscio, F., Carrasco, G., Seposo, X., Nunes, B., Madureira, J., Holobaca, I.-
 898 H., Scovronick, N., Acquafatta, F., Forsberg, B., Åström, C., Ragettli, M. S., Guo,
 899 Y.-L. L., Chen, B.-Y., Li, S., Colistro, V., Zanobetti, A., Schwartz, J., Dung, D.
 900 V., Armstrong, B., and Gasparrini, A.: Geographical Variations of the Minimum
 901 Mortality Temperature at a Global Scale: A Multicountry Study, *Environ.*
 902 *Epidemiol.*, 5, e169, <https://doi.org/10.1097/EE9.000000000000169>, 2021.
 903
 904 Turnock, S. T., Allen, R., Archibald, A. T., Dalvi, M., Folberth, G., Griffiths, P.
 905 T., Keeble, J., Roberston, E., and O'Connor, F. M.: The future climate and air
 906 quality response from different near-term climate forcer, climate, and land-use
 907 scenarios using UKESM1, *Earth's Future*, 10, e2022EF002687,
 908 <https://doi.org/10.1029/2022EF002687>, 2022.
 909
 910 van der Werf, G. R., Randerson, J. T., Giglio, L., van Leeuwen, T. T., Chen, Y.,
 911 Rogers, B. M., Mu, M., van Marle, M. J. E., Morton, D. C., Collatz, G. J.,
 912 Yokelson, R. J., and Kasibhatla, P. S.: Global fire emissions estimates during
 913 1997–2016, *Earth Syst. Sci. Data*, 9, 697–720, [https://doi.org/10.5194/essd-9-](https://doi.org/10.5194/essd-9-697-2017)
 914 [697-2017](https://doi.org/10.5194/essd-9-697-2017), 2017.
 915
 916 Wang, P., Yang, Y., Li, H., Chen, L., Dang, R., Xue, D., Li, B., Tang, J., Leung,
 917 L. R., and Liao, H.: North China Plain as a hot spot of ozone pollution
 918 exacerbated by extreme high temperatures, *Atmos. Chem. Phys.*, 22, 4705–
 919 4719, <https://doi.org/10.5194/acp-22-4705-2022>, 2022.
 920
 921 Wang, P., Yang, Y., Xue, D., Ren, L., Tang, J., Leung, L. R., and Liao, H.:
 922 Aerosols overtake greenhouse gases causing a warmer climate and more
 923 weather extremes toward carbon neutrality, *Nat. Commun.*, 14, 7257,
 924 <https://doi.org/10.1038/s41467-023-42891-2>, 2023.
 925
 926 Wang, Y., Li, K., Chen, X., Yang, Z., Tang, M., Campos, P. M. D., Yang, Y.,
 927 Yue, X., and Liao, H.: Revisiting the high tropospheric ozone over southern
 928 Africa: role of biomass burning and anthropogenic emissions, *Atmos. Chem.*
 929 *Phys.*, 25, 4455–4475, <https://doi.org/10.5194/acp-25-4455-2025>, 2025.
 930
 931 Wang, Y., Yang, Y., Yuan, Q., Li, T., Zhou, Y., Zong, L., Wang, M., Xie, Z., Ho,
 932 H. C., Gao, M., Tong, S., Lolli, S., and Zhang L.: Substantially underestimated
 933 global health risks of current ozone pollution, *Nat. Commun.*, 16, 102,
 934 <https://doi.org/10.1038/s41467-024-55450-0>, 2025.
 935
 936 Williams, J. E., Scheele, M. P., van Velthoven, P. F. J., Cammas, J.-P., Thouret,
 937 V., Galy-Lacaux, C., and Volz-Thomas, A.: The influence of biogenic emissions
 938 from Africa on tropical tropospheric ozone during 2006: a global modeling study,
 939 *Atmos. Chem. Phys.*, 9, 5729–5749, <https://doi.org/10.5194/acp-9-5729-2009>,
 940 2009.



941
 942 Wei, J., Li, Z., Li, K., Dickerson, R., Pinker, R., Wang, J., Liu, X., Sun, L., Xue,
 943 W., and Cribb, M.: Full-coverage mapping and spatiotemporal variations of
 944 ground-level ozone (O₃) pollution from 2013 to 2020 across China, *Remote*
 945 *Sens. Environ.*, 270, 112775, <https://doi.org/10.1016/j.rse.2021.112775>, 2022.
 946
 947 Xu, H., Yu, H., Xu, B., Wang, Z., Wang, F., Wei, Y., Liang, W., Liu, J., Liang, D.,
 948 Feng, Y., and Shi, G.: Machine learning coupled structure mining method
 949 visualizes the impact of multiple drivers on ambient ozone, *Commun. Earth*
 950 *Environ.*, 4, 265, <https://doi.org/10.1038/s43247-023-00932-0>, 2023.
 951
 952 Xu, Z., Han, Y., Tam, C. Y., Yang, Z., and Fu, C.: Bias-corrected CMIP6 global
 953 dataset for dynamical downscaling of the historical and future climate (1979–
 954 2100), *Sci. Data*, 8, 293, <https://doi.org/10.1038/s41597-021-01079-3>, 2021.
 955
 956 Yan, Y., Cabrera-Perez, D., Lin, J., Pozzer, A., Hu, L., Millet, D. B., Porter, W.
 957 C., and Lelieveld, J.: Global tropospheric effects of aromatic chemistry with the
 958 SAPRC-11 mechanism implemented in GEOS-Chem version 9-02, *Geosci.*
 959 *Model Dev.*, 12, 111–130, <https://doi.org/10.5194/gmd-12-111-2019>, 2019.
 960
 961 Yang, Y., Li, M., Wang, H., Li, H., Wang, P., Li, K., Gao, M., and Liao, H.: ENSO
 962 modulation of summertime tropospheric ozone over China, *Environ. Res. Lett.*,
 963 17, 034020, <https://doi.org/10.1088/1748-9326/ac54cd>, 2022.
 964
 965 Yue, X., Unger, N., Harper, K., Xia, X., Liao, H., Zhu, T., Xiao, J., Feng, Z., and
 966 Li, J.: Ozone and haze pollution weakens net primary productivity in China,
 967 *Atmos. Chem. Phys.*, 17, 6073–6089, [https://doi.org/10.5194/acp-17-6073-](https://doi.org/10.5194/acp-17-6073-2017)
 968 2017, 2017.
 969
 970 Ziemke, J. R., Chandra, S., Duncan, B. N., Schoeberl, M. R., Torres, O., Damon,
 971 M. R., and Bhartia, P. K.: Recent biomass burning in the tropics and related
 972 changes in tropospheric O₃, *Geophys. Res. Lett.*, 36, 15,
 973 <https://doi.org/10.1029/2009GL039303>, 2009.
 974
 975 Ziemke, J. R., Oman, L. D., Strode, S. A., Douglass, A. R., Olsen, M. A.,
 976 McPeters, R. D., Bhartia, P. K., Froidevaux, L., Labow, G. J., Witte, J. C.,
 977 Thompson, A. M., Haffner, D. P., Kramarova, N. A., Frith, S. M., Huang, L.-K.,
 978 Jaross, G. R., Seftor, C. J., Deland, M. T., and Taylor, S. L.: Trends in global
 979 tropospheric ozone inferred from a composite record of
 980 TOMS/OMI/MLS/OMPS satellite measurements and the MERRA-2 GMI
 981 simulation, *Atmos. Chem. Phys.*, 19, 3257–3269, [https://doi.org/10.5194/acp-](https://doi.org/10.5194/acp-19-3257-2019)
 982 19-3257-2019, 2019.
 983



984 Zunckel, M., Koosailee, A., Yarwood, G., Maure, G., Venjonoka, K., van
985 Tienhoven, A. M., and Otter, L.: Modelled surface ozone over southern Africa
986 during the Cross Border Air Pollution Impact Assessment Project, Environ.
987 Modell. Softw., 21, 911–924, <https://doi.org/10.1016/j.envsoft.2005.04.004>,
988 2006.
989



990 **Table 1.** Details of the data used in this study.

Dataset type	Variable	Description	Spatial resolution	Temporal resolution	Time period	Data source
O ₃	O ₃	Near-surface ozone concentrations	2°×2.5°	Monthly	2000–2019 (historical)	GEOS-Chem simulations
Meteorology	T_2m	Air temperature at 2 meters	2°×2.5°	Monthly	2000–2019 (historical) 2020–2054 (future)	MERRA-2 (historical) Adjusted CMIP6 (future)
	T_850	Air temperature at 850 hPa				
	T_500	Air temperature at 500 hPa				
	U_850	Zonal wind at 850 hPa				
	U_500	Zonal wind at 500 hPa				
	V_850	Meridional wind at 850 hPa				
	V_500	Meridional wind at 500 hPa				
	RH	Near-surface relative humidity				
	PRECP	Precipitation rate				
	CLT	Total cloud cover				
	RSDS	Incoming shortwave radiation at the surface				
	SLP	Sea level pressure				
Emission		Nitric oxide from soil sources	2°×2.5°	Monthly	2019	CEDS (Anthropogenic) GFED4 (Biomass burning) MEGAN2.1 (Biogenic) NOAA GMD for CH ₄
		Nitric oxide from lightning sources				
	NO _x	Nitric oxide from anthropogenic sources			2000–2019 (historical) 2019 (future)	
		Nitric oxide from biomass burning				
	CO	Carbon monoxide from anthropogenic sources				
		Carbon monoxide from biomass burning			2019 (historical) 2020–2054 (future)	
	CH ₄	Surface methane concentration				
	NMVOCs	Non-methane volatile organic compounds from anthropogenic sources				
		Non-methane volatile organic compounds from biomass burning				
		Non-methane volatile organic compounds from biogenic sources				
Land use	LC	Land cover	300 m×300 m	Monthly	2000–2019 (historical) 2019 (future)	ESA CCI
	NDVI	Normalized Difference Vegetation Index	0.05°×0.05°		AVHRR	
Topography	TOPO	Digital elevation model	90 m×90 m	-	2010	SRTM
Population	POP	Population density	1 km×1 km	-	2010	Land Scan

991

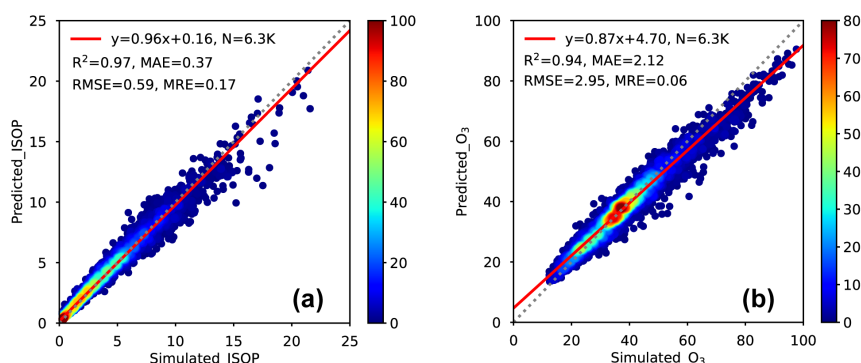


Figure 1. Density plot of GEOS-Chem model simulated vs. Random Forest model predicted monthly (a) biogenic isoprene emissions ($\text{g/m}^2/\text{yr}$) and (b) near-surface O_3 concentrations (ppb) in 2010 over Africa. The gray dotted and red lines are the 1:1 lines and linear regression lines, respectively. Statistical metrics including correlation of determination (R^2 , unitless), root mean square error (RMSE, $\text{g/m}^2/\text{yr}$ or ppb), mean absolute error (MAE, $\text{g/m}^2/\text{yr}$ or ppb), and mean relative error (MRE, %) are given at the top of each panel.

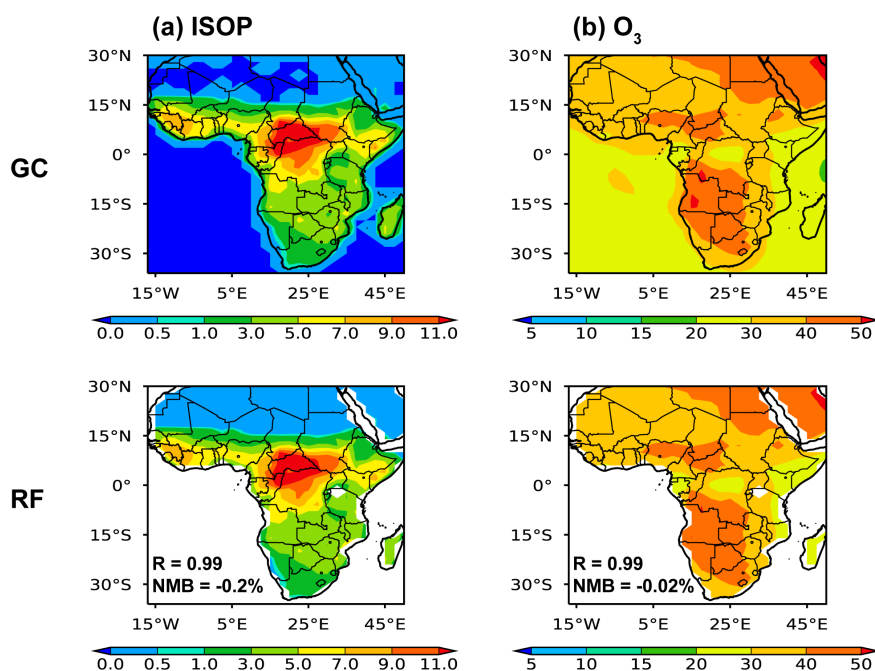


Figure 2. Spatial distributions of (a) biogenic isoprene emissions (ISOP, g/m²/yr) and (b) near-surface O₃ concentrations (ppb) derived from GEOS-Chem model (GC) and Random Forest model (RF) over Africa in 2000–2019. The correlation coefficient (R) between simulated and predicted O₃ and the normalized mean bias (NMB= (Simulated – Predicted) / Predicted ×100 %) are given at the bottom left of panels.

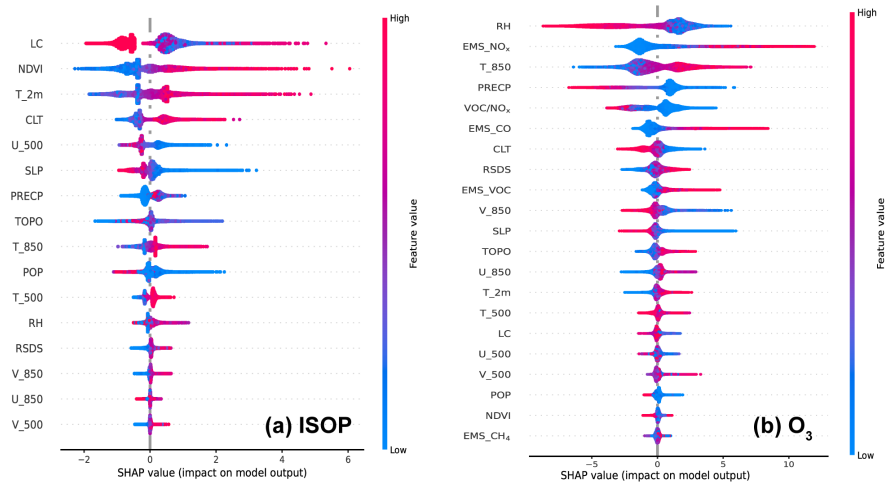
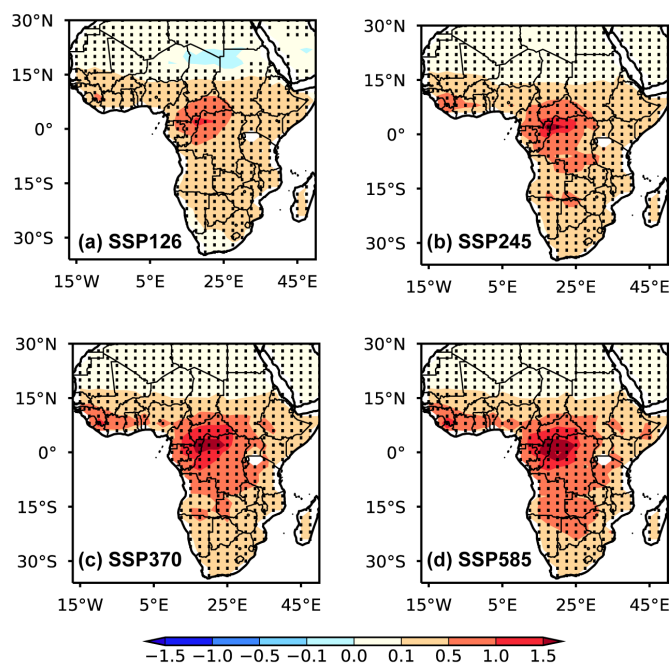


Figure 3. Main and interactive effects of major input features on projections of (a) biogenic isoprene emissions (ISOP) and (b) near-surface O₃ concentrations over Africa from Shapley Additive explanation (SHAP) analysis. The relative importance of selected independent features is shown in the descending order. A positive (negative) SHAP value suggests a positive (negative) contribution.



1019

1020

1021 **Figure 4.** Spatial distributions of differences in scenario-driven biogenic
 1022 isoprene emissions ($\text{g/m}^2/\text{yr}$) between 2050–2054 and 2020–2024 under (a)
 1023 SSP1-2.6, (b) SSP2-4.5, (c) SSP3-7.0 and (d) SSP5-8.5 scenarios predicted
 1024 by the RF model. The shaded areas indicate that the differences are statistically
 1025 significant at the 90% confidence level.

1026

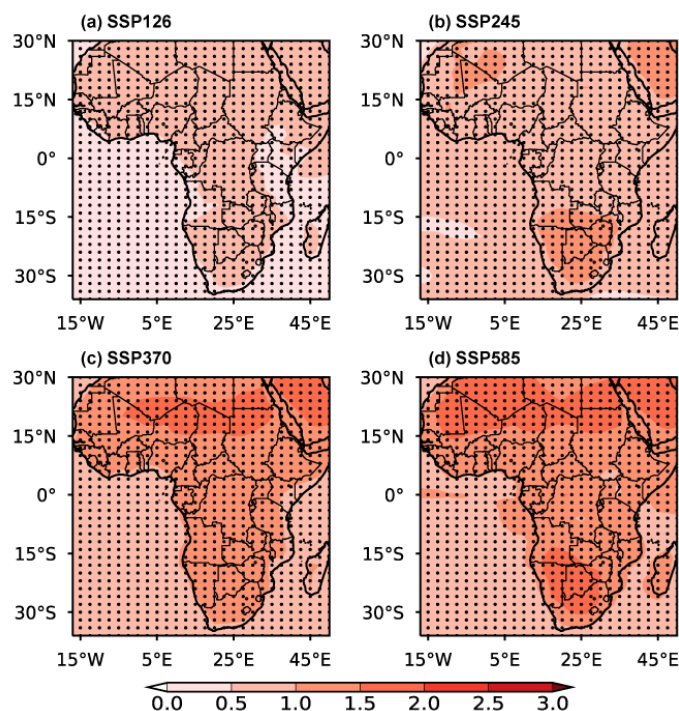


Figure 5. Spatial distributions of differences in the CMIP6 multi-model mean of air temperature at 2m (T_{2m} , K) between 2050–2054 and 2020–2024 over Africa under (a) SSP1-2.6, (b) SSP2-4.5, (c) SSP3-7.0 and (d) SSP5-8.5 scenarios. The shaded areas indicate that the differences are statistically significant at the 90% confidence level.

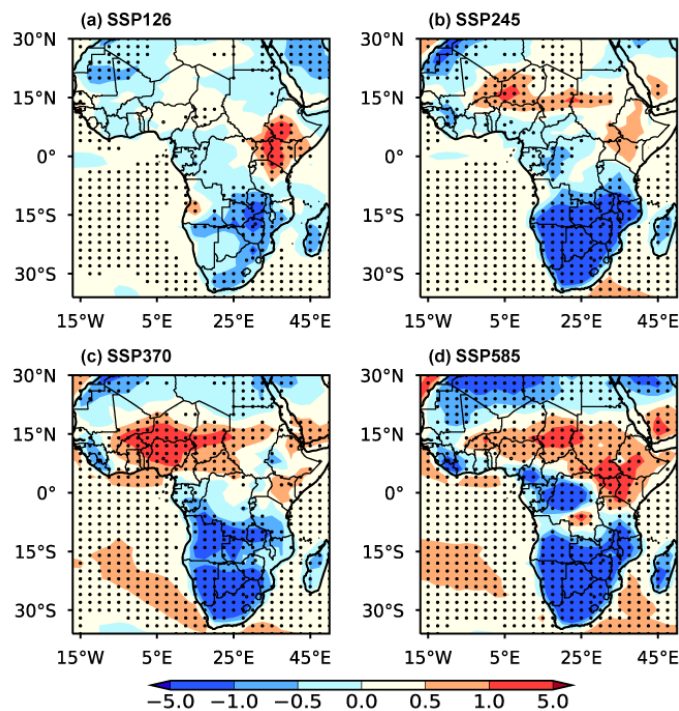


Figure 6. Spatial distributions of differences in the CMIP6 multi-model mean of relative humidity (RH, %) between 2050–2054 and 2020–2024 over Africa under (a) SSP1-2.6, (b) SSP2-4.5, (c) SSP3-7.0 and (d) SSP5-8.5 scenarios. The shaded areas indicate that the differences are statistically significant at the 90% confidence level.

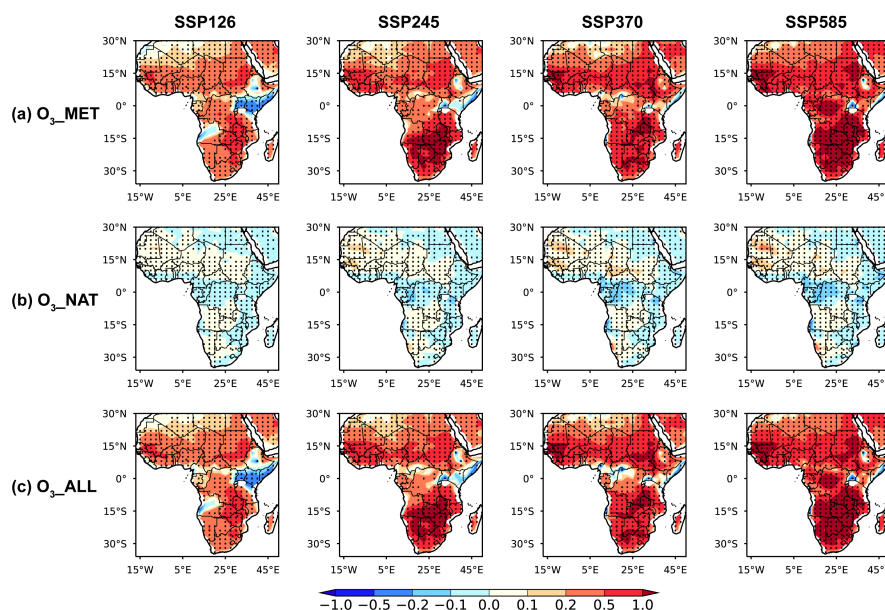


Figure 7. Spatial distributions of differences in RF-predicted near-surface O_3 concentrations (ppb) over Africa in response to (a) changes in meteorological fields (O_3_MET), (b) changes in biogenic isoprene emissions (O_3_NAT), and (c) both changes (O_3_ALL) between 2050–2054 and 2020–2024 under SSP1-2.6, SSP2-4.5, SSP3-7.0 and SSP5-8.5 scenarios. The shaded areas indicate that the differences are statistically significant at the 90% confidence level.

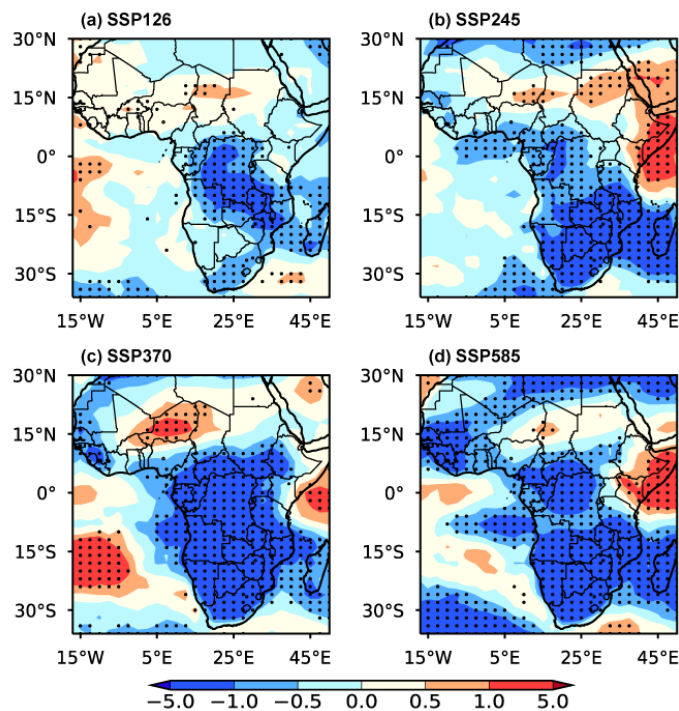


Figure 8. Spatial distributions of differences in the CMIP6 multi-model mean of total cloud cover (CLT, %) between 2050–2054 and 2020–2024 over Africa under (a) SSP1-2.6, (b) SSP2-4.5, (c) SSP3-7.0 and (d) SSP5-8.5 scenarios. The shaded areas indicate that the differences are statistically significant at the 90% confidence level.

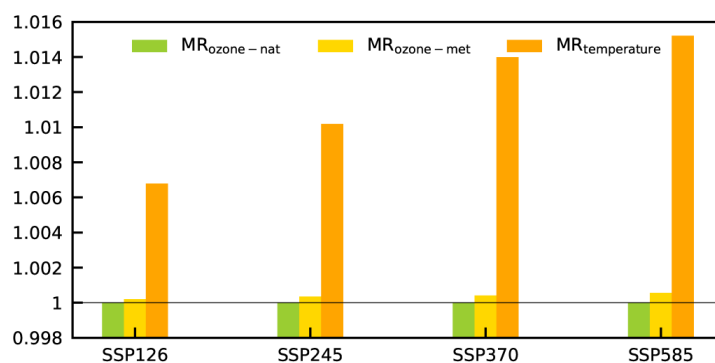
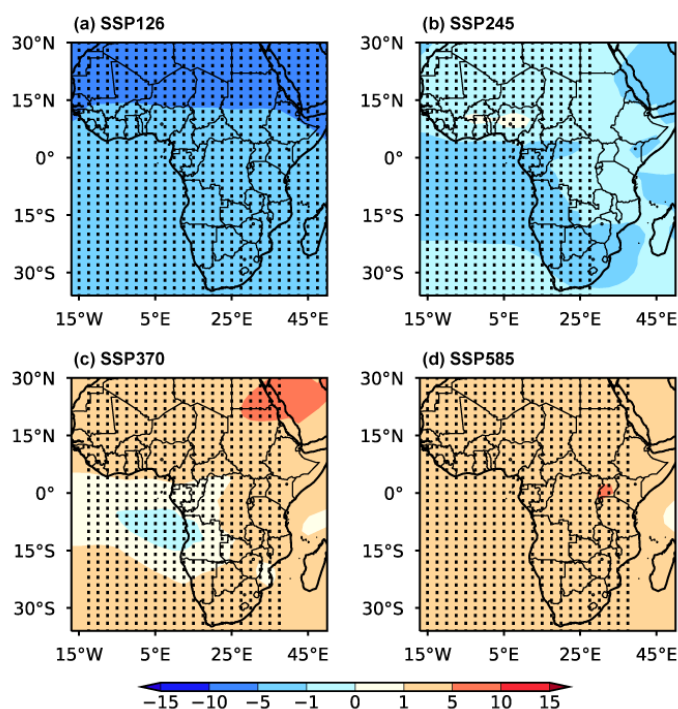


Figure 9. Mortality ratio over Africa due to climate-driven changes in O₃ levels related to natural emissions (MR_{ozone-nat}), O₃ levels related to meteorological fields (MR_{ozone-met}), and air temperature (MR_{temperature}) in 2050–2054 relative to 2020–2024 under SSP1-2.6, SSP2-4.5, SSP3-7.0 and SSP5-8.5 scenarios.



1067
 1068

1069 **Figure 10.** Spatial distributions of differences in near-surface O_3 concentrations
 1070 (ppb) between 2050–2054 and 2020–2024 under (a) SSP1-2.6, (b) SSP2-4.5,
 1071 (c) SSP3-7.0 and (d) SSP5-8.5 scenario obtained from CMIP6 multi-model
 1072 simulations. The shaded areas indicate that the differences are statistically
 1073 significant at the 90% confidence level.